

Journal of Materials Chemistry A

Understanding the Catalysis of Noble Metals in Reduction of Iron Oxide by Hydrogen: Insights from DFT Calculations

Journal:	Journal of Materials Chemistry A
Manuscript ID	TA-ART-07-2024-004793.R1
Article Type:	Paper
Date Submitted by the Author:	15-Sep-2024
Complete List of Authors:	Tang, Qiming; University of Maryland at College Park, Materials Science & Engineering Lei, Xueling; Jiangxi Normal University, Department of Physics Zhang, Yongliang; University of South Carolina System, Mechanical Engineering Lu, Jiaxin; University of South Carolina System, Department of Mechanical Engineering Huang, Kevin; University of South Carolina System, Department of Mechanical Engineering

SCHOLARONE™ Manuscripts

Understanding the Catalysis of Noble Metals in Reduction of Iron Oxide by Hydrogen: Insights from DFT Calculations

Qiming Tang,¹ Xueling Lei^{2*}, Yongliang Zhang¹, Jiaxin Lu¹, Kevin Huang^{1*}

Department of Mechanical Engineering, University of South Carolina, Columbia, SC 29201,

USA

² Department of Physics, Jiangxi Normal University, Nanchang, Jiangxi 330022, China.

*Corresponding author: e-mail: huang46@cec.sc.edu xueling@mail.ustc.edu.cn

Abstract

Fe/FeO_x redox couples have been widely used as an oxygen carrier for redox devices such as chemical looping reactors and solid oxide iron-air battery (SOIAB) because of their low cost and high oxygen capacity. However, a critical challenge is the sluggish reduction kinetics of FeO_x in the intermediate temperature range, significantly limiting the devices' achievable efficiency and service life. Here, we report on a combined theoretical and experimental study on the catalytic effect of noble metals (Ir, Ru, Rh, Pd and Pt) on the H_2 -reduction kinetics of FeO_x . We first use density functional theory (DFT) to calculate the electron projected density of states (PDOS) near Fermi level (E_F) of several noble metal (Ir, Pd, Ru, Rh, Pd)/ Fe_3O_4 systems. We reveal that Ir offers the highest PDOS near E_F among all noble metals studied, which provides abundant electrons for efficient cleavage of O-Fe bonds and low-energy dissociation of H_2 molecules, thus resulting in significantly boosted reduction kinetics of Fe_3O_4 . Experimentally, the results of temperature programmed reduction and SOIAB performance testing corroborate the theoretical predictions.

Keywords: Iron oxide reduction; catalysis; noble metals; oxygen activation; hydrogen dissociation.

I. Introduction

Development of Long Duration Energy Storage (LDES) technology is significant to fully utilize renewable energy and reduce our dependence on fossil fuels. 1-5 It is also crucial for the stability and reliability of our future smart energy grid systems. Various types of rechargeable batteries that are currently in use or under development for LDES applications include lithium-ion batteries (LIBs), redox flow batteries (RFBs) and metal-air batteries, et.al. 6-9 However, traditional LIBs are limited in extending storage durations beyond 10 hours due to the high scaling-up cost, not to mention the safety concern over clustered Li-ion battery systems. RFBs are scalable and safer compared to LIBs, but low in energy density and energy efficiency. Conventional alkaline Fe-air batteries have recently been demonstrated at a commercial scale, but challenges such as high cathodic overpotential, hydrogen evolution and anode passivation remain to be addressed.

Recently, a new type of ceramic solid oxide iron-air batteries (SOIABs) has been shown with competitive performance for LDES.¹⁰⁻¹⁶ This new type of all solid-state battery is operated on oxide-ion chemistry, in which the chemical energy of oxygen in the form of O²⁻ is reversibly stored in an energy dense Fe/FeO_x redox couple integrated within the anode chamber of a reversible solid oxide cell (RSOC). The electrochemical reactions occur at the RSOC, while the chemical redox reaction between Fe, H₂O, H₂ and FeO_x is at the Fe/FeO_x bed. In the discharge mode, H₂ is consumed at the RSOC (in solid oxide fuel cell mode, SOFC) to generate electricity and H₂O. The generated H₂O is immediately reacted with Fe to produce more H₂ to sustain the SOFC power generation. In the charge mode, H₂O is split into H₂ at the RSOC (in solid oxide electrolysis cell mode, SOEC); the latter then reduces FeO_x to metallic Fe and produces H₂O to sustain the SOEC operation. Therefore, the direction of the global reaction is driven by the flow of electrical current during cycles. An ideal Fe-based energy storage redox couple for SOIABs must have good activity

for the desirable redox reaction at elevated temperature in H_2/H_2O environment and exhibit durability over repeated cycles. Based on the previous modeling and experimental data, FeO_x such as Fe_3O_4 suffers sluggish H_2 -reduction kinetics at SOIAB operation temperature ($500^{\circ}C-600^{\circ}C$), 17 resulting in low round trip efficiency and low energy density, especially at higher current densities. One strategy to improve H_2 -reduction kinetics and battery performance is to catalyze the slow kinetics by noble metal (NM) particles. Previous reports have shown that iridium (Ir) is a good catalyst for iron reduction process. $^{13-14}$ However, there is a lack of fundamental understandings for the enhanced kinetics mechanisms. In this work, we aim to bridge this scientific gap by employing density functional theory (DFT) to theoretically investigate the O activation and H_2 dissociation processes on the surface of NMs (NM= Ir, Ru, Rh, Pd and Pt)/ Fe_3O_4 complexes. We specifically calculate the electron project density of states (PDOS) near Femi level (E_F) of different noble metals on the surface of Fe_3O_4 to unveil the underlying reasons for the boosted reduction kinetics. We then use temperature programed reduction (TPR) and SOIAB battery testing to verify the theoretical predictions.

II. Results and Discussion

2.1 Geometric and electronic structures of M-Fe₃O₄ (M=Ir, Ru, Rh, Pd and Pt)

To understand fundamentally the catalytic mechanisms of NMs on the reduction kinetics of FeO_x , identifying the relation between the NM's electronic structure and catalytic activity is a key. For H_2 -reduction of FeO_x , it is reasonable to assume that H_2 will be first absorbed on the FeO_x surface and then dissociated over coordinately unsaturated transition sites of the FeO_x surface. Therefore, the presence of electron-rich NMs in the neighborhood will play an important role in the reduction process. According to previous reports and Baur-Glaessner's equilibrium diagram of the Fe-O-H

system, 18 under SOIAB operating conditions, Fe₃O₄ is the major oxide phase involved in the redox cycling. Furthermore, previous reports indicate that the (111) surface of Fe₃O₄ is the most stable. 19 Therefore, the (111) surface was built for all DFT calculations to study O activation and H₂ dissociation.

The optimized lowest energy (111) surface structures of Fe₃O₄ before and after NM introduction, along with the PDOS are shown in Figure 1. The potential binding sites of NM on the substrate have been investigated, and the optimized structures, along with their relative energies, are shown in Figure S1, Supporting Information. For pristine Fe₃O₄ (111), Figure 1a (left) illustrates that the optimized Fe₃O₄ (111) structure contains one Fe atom bonding with three O atoms and one O atom bonding with three Fe atoms, while the PDOS plot (right) indicates that the electronic states near E_F are mainly contributed from Fe atom with low PDOS near E_F. After introducing Ir to the surface of Fe₃O₄ (111), Figure 1b reveals that one O in Fe₃O₄ (111) surface is activated, that is, two of the Fe-O bonds are broken, with an O atom protruding from the surface, concurrently forming one Ir-O bond. In addition, the calculated PDOS of the broken O, see Figure S2, depicts a new state appeared near E_F, further confirming the activation of O atom. The broken dangling O is catalytically active to form an OH group with the spillover H during the reduction process. Furthermore, the PDOS plot in Figure 1b shows a significant change compared to that of pure Fe₃O₄ (111), i.e., the introduction of Ir gives rise to occupied states of Ir near E_F in both spin up and spin down states, making electrons readily available for the subsequent H₂ dissociation to reduce Fe₃O₄ (111).

However, it is not the case for Ru/Fe₃O₄ (111). After introducing Ru, Figure 1c indicates that there is almost no occupied electronic state near the E_F . In other words, nearly all electrons in Ru are used for activating two O atoms in Fe₃O₄ (111) surface, see Figure S2, leaving insufficient

electrons for H_2 dissociation. Similarly for Rh and Pt, Figure 1d and 1e indicate that one O atom in Fe_3O_4 (111) is activated, but less electronic states occupied near E_F are present, leaving insufficient electrons for H_2 molecule dissociation. As for the Pd/Fe₃O₄ (111), Figure 1f shows no activated O atom on the surface, so it may not be catalytically active at all. Therefore, Ir/Fe_3O_4 is expected to exhibit the best catalytic activity toward Fe_3O_4 reduction by H_2 among the all of NM catalysts studied because it provides enough electrons not only for activating O atom (by breaking Fe-O bonds) on the Fe_3O_4 (111) surface, but also for the subsequent H_2 dissociation.

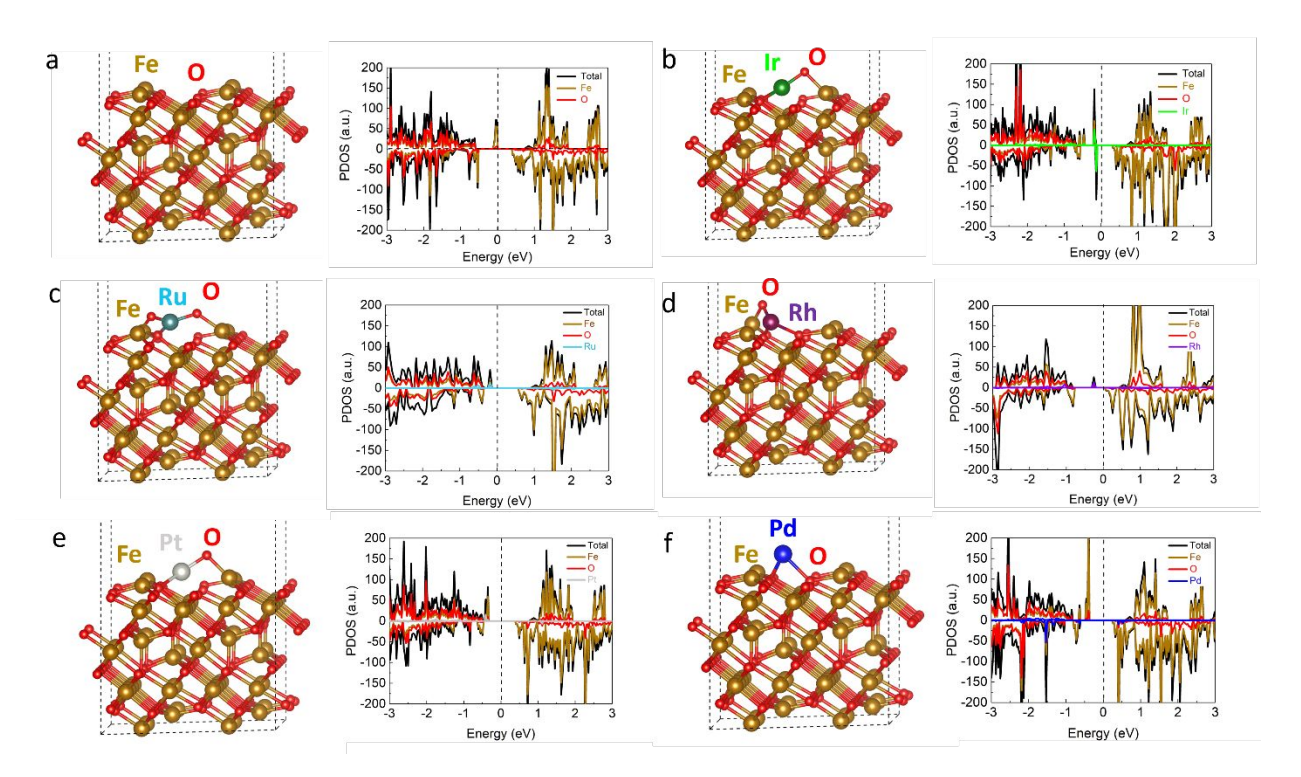


Figure 1. Optimized surface structure and corresponded projected density of states of (a) pristine Fe₃O₄, (b) Ir/Fe₃O₄, (c) Ru/Fe₃O₄, (d) Rh/Fe₃O₄, (e) Pt/Fe₃O₄, (f) Pd/Fe₃O₄. The Fermi level is set to be zero with a dashed line as a guide.

Given that *d*-band center can be used to predict the catalytic activity of NMs, we also calculated the *d*-band center of different NMs on Fe₃O₄ (111) and the corresponding charge transfer (Δ Q) during oxygen activation; the data are shown in Table S1. Next to Pd, Ir exhibits the highest d-

band center (-3.49 eV), closer to the lowest unoccupied molecular orbital (LUMO) of free H_2 , see Table S2. This finding suggests a lower energy barrier for electron transfer from Ir to H_2 and higher catalytic activity toward H_2 dissociation. Even though Pd has a higher d-band center than Ir, it cannot activate the O atom as shown in Figure 1f. Therefore, it is reasonable to conclude that the high catalytic activity of Ir toward Fe_3O_4 (111) reduction is derived from the combined effect of effective O activation and subsequent H_2 dissociation, all of which is enabled by the rich PDOS of Ir near E_F .

To further analyze the electronic structure of Ir/Fe_3O_4 under H_2 environment, an optimized structure of one H_2 molecule on the Ir/Fe_3O_4 (111) surface has been obtained, see Figure 2a; the corresponding PDOS for Ir, activated O and H_2 is shown in Figure 2b. The abundant electronic states appear near E_F because of the extra electrons released by Ir, leading to high activation for H_2 dissociation after H_2 adsorption (with an adsorption energy of 0.04 eV). In contrast, only a few electronic states of Ru can be found near E_F on the Ru/Fe_3O_4 (111) surface, see Figure 2c and 2d. Table S1 indicates that Ru has the highest ΔQ value with two activated O atoms; however, no more electrons are available to dissociate H_2 molecules. Therefore, lower catalytic activity for H_2 dissociation is expected for Ru. Other noble metals (Rh and Ru) only show one O activation and low occupied electron state near E_F , implying even worse catalytic activity than Ir and Ru. Therefore, we will focus on Ir/Fe_3O_4 and Ru/Fe_3O_4 systems in the following discussion.

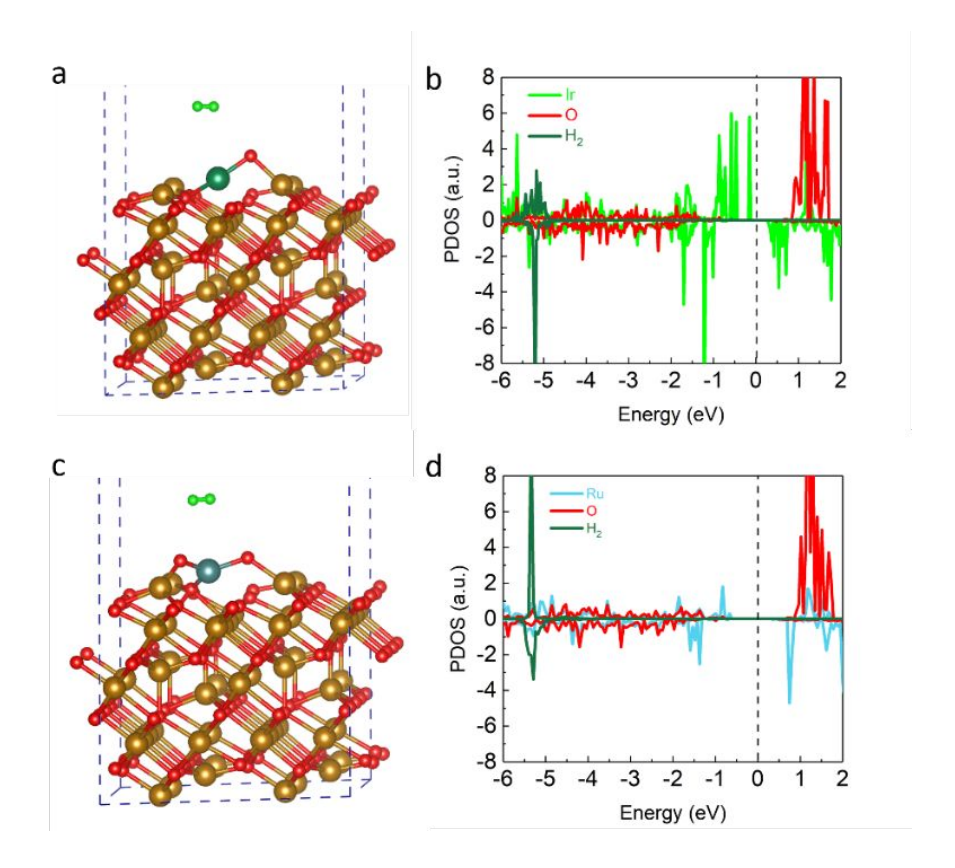


Figure 2. (a) Optimized structure of Ir/Fe₃O₄ under H₂ environment; (b) the corresponding PDOS of Ir (bright green), activated O (red) and H₂ (green); (c) Optimized structure of Ru/Fe₃O₄ under H₂ environment; (d) the corresponding PDOS of Ru (fluorescent blue), activated O (red) and H₂ (green).

2.2 Dynamics of H_2 dissociation on M-Fe₃O₄ (111) (M=Ir and Ru) surface

To further elucidate the interactions between H_2 and Fe_3O_4 (111) after introducing NMs, we also simulated H_2 adsorption, dissociation, and migration steps on the NM-decorated Fe_3O_4 (111) surface. Figure 3a shows the energy profile and the H-H bond length as function of the distance of H_2 molecule from the surface (defined as the distance between H atom and Ir atom, H-Ir distance) along with the optimized structures at different stages. When H_2 is close to the surface, the following steps take place: 1) physical adsorption of H_2 on surface of an Ir atom; 2) dissociation into two chemisorbed H atoms, where the H-H bond length increases sharply and then breaks; 3)

H atom migration along the surface of Ir-Fe₃O₄ (111), where one of H atoms migrates from the Ir atom to the adjacent activated O atom. It is interesting to note from Figure 3a that when H_2 approaches the surface of Ir/Fe₃O₄ (111), the energy increases and so does the H-H length, suggesting that the H-H bond is elongated. When the H-Ir distance reaches 1.6 Å, the H-H bond starts breaking, and new bonds between H and O are formed with an energy barrier of 0.71 eV; the latter is much lower than 1.24 eV in the case of Ru/Fe₃O₄ (111) surface, see Figure 3b, suggesting Ir can promote the H_2 dissociation more effectively than Ru. The Ir's high electronic density still available after O activation is the fundamental reason for the high activity toward H_2 dissociation.

Furthermore, it is worth noting that the energy at a H-Ir distance of 1.6 Å (final state of the reaction) is lower than that of H_2 in the gas phase (initial state of the reaction). Conversely, for the Ru/Fe_3O_4 (111) surface, the energy of the reaction's final state is higher than that of its initial state. This indicates that the dissociation of H_2 is exothermic on the Ir/Fe_3O_4 (111) surface, whereas it is endothermic on the Ru/Fe_3O_4 (111) surface. The disparity in energy primarily arises from the differing interactions between hydrogen and either Ir or Ru. On the Ir/Fe_3O_4 (111) surface, the energy barrier for the reverse reaction is higher than that for the forward reaction, resulting in a very stable state once the H_2 molecule dissociates. In contrast, on the Ru/Fe_3O_4 (111) surface, the energy barrier for the reverse reaction is lower than that for the forward reaction, suggesting that the dissociation state is relatively less stable. These observations further substantiate that Ir doping outperforms Ru doping in terms of catalytic performance towards H_2 dissociation.

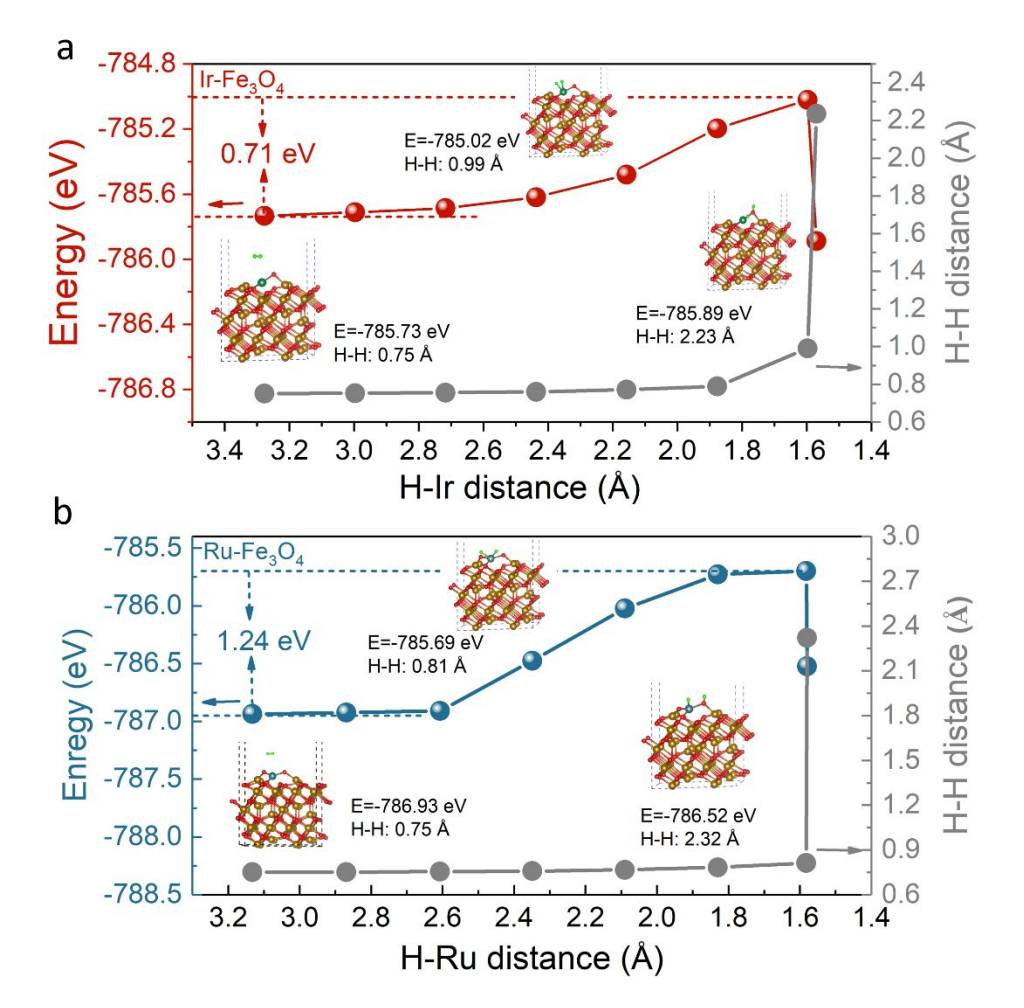


Figure 3. Simulations of H₂ migration during dissociation: the changes of total energy and H-H bond length when H₂ moves from far enough distance to the surface on (a) Ir/Fe₃O₄ surface and (b) Ru/Fe₃O₄ surface. The corresponding optimized structures for the most favorable path for dissociation of H₂ are also shown in the insets.

2.3 Phase composition and morphologies of Fe-based energy materials

To verify the theoretical predictions, we prepared the baseline and NM-added Fe₂O₃/ZrO₂ samples. Note that Fe₂O₃ will be reduced Fe₃O₄ under the SOIAB operating conditions. The phase purity of as-prepared different noble metals added Fe₂O₃/ZrO₂ is confirmed by XRD patterns shown in Figure 4a. Here, ZrO₂ acts as an inert oxide support to suppress the agglomeration of Fe particles

during reduction and oxidation, which has been reported in our previous reports. ^{18, 20} After mixing with NM oxides, the peaks shift slight to the right because of the strains produced in iron oxide lattice after incorporation of NMs due to the difference in atomic sizes between the two. In this case, compressive strains are created, causing a decrease in the lattice parameters and XRD peaks shifting to higher angles. Only IrO₂ and RuO₂ peaks appear, and no other extra peaks were found, confirming that there is no reaction between NM oxides and Fe₂O₃/ZrO₂. However, there is no obvious Rh, Pt and Pd-species related peaks observed, which could be due to their low crystallinity.

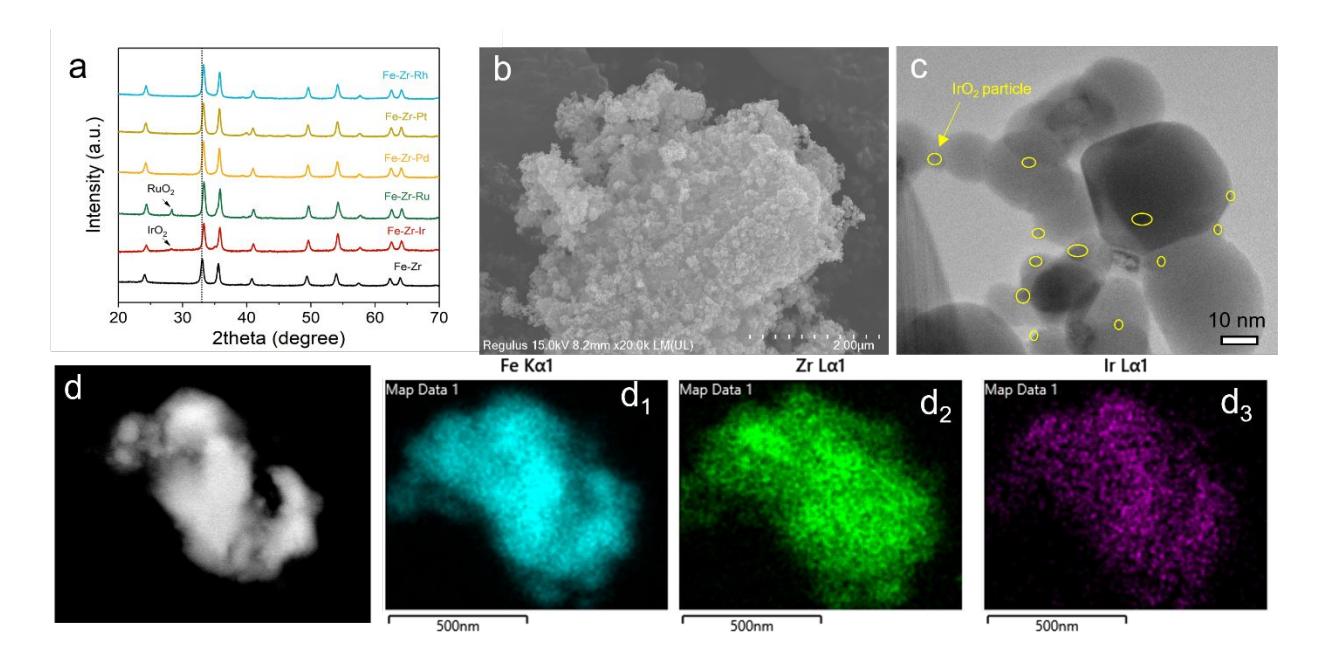


Figure 4. (a) XRD patterns of the as-prepared noble metal added Fe_2O_3/ZrO_2 . (b) SEM image of $Ir-Fe_2O_3/ZrO_2$ as an example; (c) TEM images of $Ir-Fe_2O_3/ZrO_2$ as an example; (d) element mapping of $Ir-Fe_2O_3/ZrO_2$ as an example.

Figure S3 shows the morphology of the pristine Fe₂O₃/ZrO₂ active material, whereas Figure 4b shows the morphology of as-prepared IrO₂-added Fe₂O₃/ZrO₂. Compared to the pristine Fe₂O₃/ZrO₂, it seems that IrO₂-Fe₂O₃/ZrO₂ exhibits more separation of particles than segregation, see Figure S4. Figure 4c of high-resolution TEM imaging further reveals abundant IrO₂

nanoparticles (~3nm) distributed uniformly on the Fe₂O₃/ZrO₂ surface. After 100-cycle in SOIAB at 550°C (the performance to be shown later), Ir (thermally decomposed from IrO₂)-Fe₂O₃/ZrO₂ only exhibits a slight coarsening, see Figure S5. In addition, the elemental mapping shown in Figure 4d suggests all elements are distributed uniformly.

2.4 Temperature Programed Reduction

Temperature Programed Reduction (TPR) was conducted on different NM-added FeO_x samples to verify the theoretical predictions, and the results are shown in Figure 5. The first peak at 100-150°C can be assigned to the reduction of NM oxides to metal under H₂ environment. The second peak at around 200-325°C comes from the first stage of reduction: Fe₂O₃ \rightarrow Fe₃O₄, while the combined peak at 400-700°C is related to Fe₃O₄ \rightarrow FeO \rightarrow Fe. After inducing NMs, the peak shape at 400-700°C changes and moves leftwards, suggesting an improved reduction kinetics. Small changes in peak shape for different NM catalysts are observed, implying the same reduction mechanisms are followed. Compared to other NMs, Ir (red line) shifts to the left to the most degree, especially for the peak at 400-700°C, meaning the best catalytic activity. It is worth noting that at 158 °C, there is a small peak in Ir-Fe₂O₃/ZrO₂, which can be attributed to the early reduction due to the improved reduction kinetics.

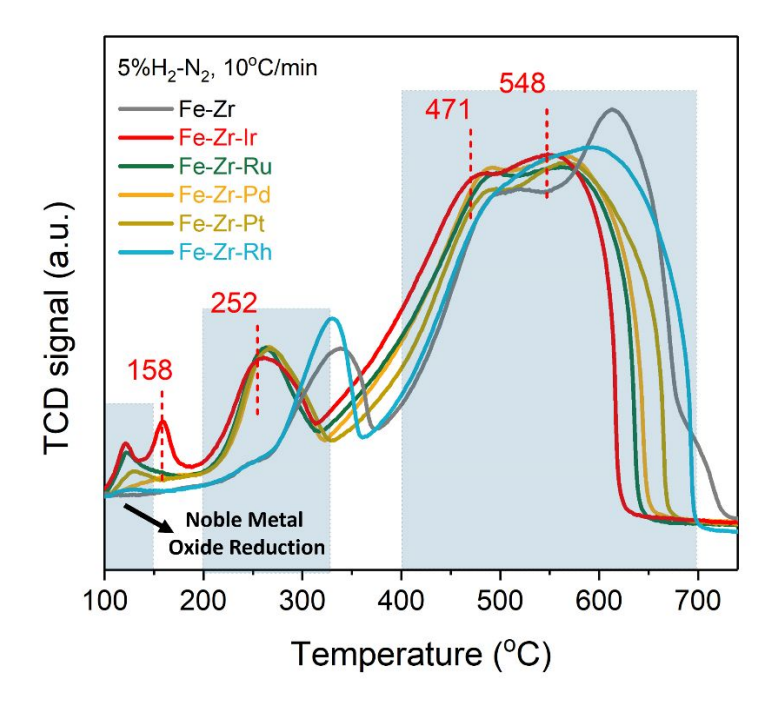


Figure 5. TPR profiles of as-prepared NM/Fe₂O₃ samples in the range of 100-700°C with a ramping rate of 10 °C/min.

2.5 Battery Performance Evaluation

To further demonstrate the improved SOIAB performance with NM-added Fe-bed, batteries with the Ir-Fe₂O₃/ZrO₂ and Ru-Fe₂O₃/ZrO₂ energy storage material were assembled and tested at 550 °C. Detailed testing procedure can be found in the experimental section as well as our early works.¹³ Note the active redox couple becomes Fe/Fe₃O₄ under SOIAB operation condition. The electrochemical performance of the solid oxide cell in SOIAB is shown in Figure S6 and the voltage profiles vs. time and corresponding Round Trip Efficiency (RTE) at a fixed iron utilization (U_{Fe} =10%) but at different current density (0.1C to 1.5C) are shown in Figure 6a and 6b. These results show that the SOIAB with the Ir-Fe₂O₃/ZrO₂ can achieve 1.5C (75 mA/cm²) at RTE = 62%, compared to RTE= 50% at 0.6C (30 mA/cm²) for the Ru-Fe₂O₃/ZrO₂; the latter also shows an obvious degradation. The specific energy density comparison shown in Figure S7 indicates that

increasing C-rate leads to a decrease in discharge energy density and increase in charge energy density as expected. However, both have a better rate performance than the baseline. Since Ir- Fe_2O_3/ZrO_2 batteries perform better than Ru- Fe_2O_3/ZrO_2 , it was further cycled for another 100 h with $U_{Fe}=5\%$ at 10 mA/cm², see Figure 6c; no significant degradation is observed. The corresponding discharge specific energy density and RTE shown in Figure 6d are 63 Wh kg⁻¹ and 90%, respectively. To achieve higher energy delivery, the battery was further cycled at higher $U_{Fe}=50\%$ and higher current density of 0.4C (20 mA/cm²), see Figure S8. After 80 hours stable operation (or 32 cycles of 2.5 hour per cycle), the IrO₂-battery exhibits a discharge energy density of 597 W h kg⁻¹-Fe at a round-trip efficiency of 80%.

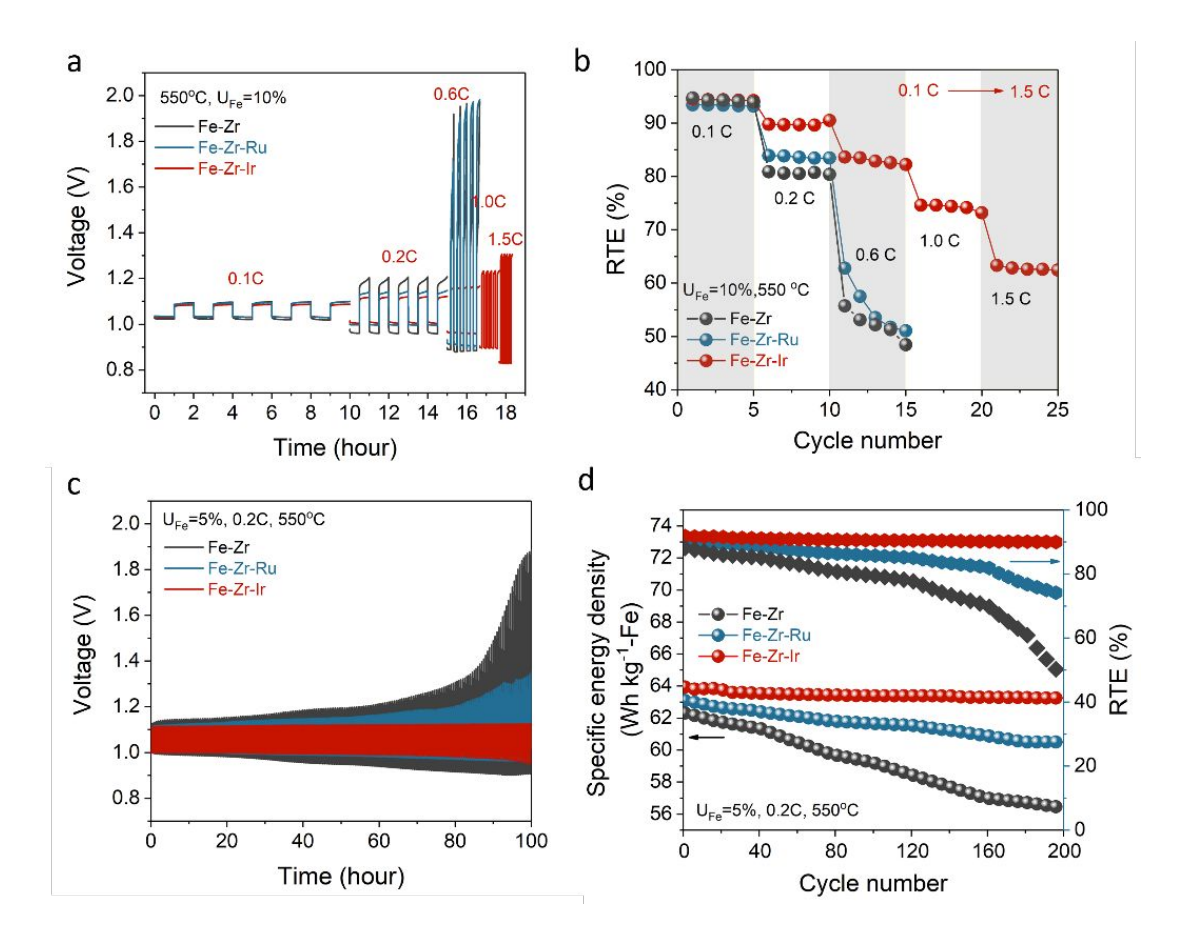


Figure 6. Electrochemical performance of SOIAB at 550°C: (a) voltage profiles versus time under different current densities (C-rate) with a fixed $U_{Fe} = 10\%$; (b) Round Trip Efficiency (RTE) versus

C-rate; (c) voltage profiles versus time at a fixed j = 10 mA cm⁻² (0.2 C) and U_{Fe}=5%; (d) the corresponding discharge specific energy density and RTE.

III. Conclusion

In summary, we have investigated noble metals (Ir, Ru, Rh, Pd and Pt) catalytic activity for Fe₃O₄ reduction using DFT calculations and experimental testing. We find that the electron PDOS near Femi level of NM plays a decisive role in the resultant catalytic activity toward Fe₃O₄ (111) reduction. Ir offers the highest PDOS among all NM catalysts studied, efficiently providing more electrons to participate in the O activation and H_2 dissociation processes for enhanced reduction kinetics. Both TPR and SOIAB results verify the theoretical predictions, i.e., for Ir-added Fe-bed material, the former indicates the earliest onset reduction temperature, while the latter shows the best electrochemical performance. The SOIAB with Ir catalyst exhibits the best performance with a discharge energy density of 597 W h kg⁻¹-Fe at RTE= 80 % at U_{Fe} =50% and 20 mA/cm² (0.4C) current density.

Methods and Computation Details

First-principles calculations. All of density functional theory (DFT) calculations were carried out by using the Vienna ab initio simulation package (VASP). The projector augmented wave (PAW) approach ²¹⁻²² was used to describe the ion-electron interaction, and the general gradient approximation (GGA) expressed by the Perdew, Burke and Ernzerhof (PBE) functional was used to treat the electronic exchange-correlation interaction.²³ A 12-layer Fe₃O₄ (111) surface with tetrahedral Fe termination was built, in which the bottom 9 layers were fixed to represent the bulk, while the top 3 layers atoms were fully relaxed. The model structures were fully optimized using

the convergence criterion of 0.01 eV/Å for the final force and 10⁻⁶ eV for the total electronic energy on Fe₃O₄ bulk and (111) surface relaxation and the plane wave cutoff was set to 500 eV, while for H₂ molecule adsorption optimizations, the convergence criterion of 0.05 eV/Å was used. The Monkhorst-Pack scheme k-points sampling was performed for integration in the first Brillouin zone, and the separation of the k-point mesh was $\sim 0.03 \text{ Å}^{-1}.24 \text{ To avoid any interlayer interactions}$ between periodic images, the vacuum region in the c directions was adopted large than 24 Å. The spin-polarized computation was performed. To better model the interactions between the adsorbed H₂ molecule and the surface, van der Waals (vdW) correction was also included in the calculations, where the DFT-D3 correction method was used in this work. ²⁵ Considering the strong *d*-electron correlation effects, the rotationally invariant density functional theory (DFT+U) approach was performed with U_{eff} =3.8 eV for Fe and U_{eff} =2.0 eV for NMs.²⁶⁻²⁷ The valence electron configurations of metals and O used in the current calculations are listed in Table S3. The selection of these valence electron configurations is a common practice for noble metal DFT modeling. ²⁸-³² The tetrahedron method with Blöchl corrections (ISMEAR =-5) was employed to calculate the projected electronic density of states (PDOS), and the VASPKIT Standard Edition 1.4.1 for data processing. 33

Fe-based energy storage material. The baseline Fe-bed (the energy storage material) is a mixture of Fe₂O₃ and ZrO₂ instead of Fe₂O₃, here the ZrO₂ acts as inert oxide support, which was synthesized by a co-precipitation method as reported previously.¹⁸ Then, the different transition metal (Ir, Ru, Rh, Pd and Pt) based Fe₂O₃/ZrO₂ were prepared by a facile impregnation method. Briefly, the as-prepared Fe₂O₃/ZrO₂ was first ball milled using a planetary ball mill (BM4X-04, COL-INT TECH) in a zirconium container for 24 h with a milling speed of 300 rpm. Then, stoichiometric transition metal precursor (Iridium III 2,4-pentanedionate (C₁₅H₂₁IrO₆), Ruthenium

acetylacetonate ($(C_5H_7O_2)_3Ru$), DiRhodium tetraacetate ($C_8H_{12}O_8Rh_2$), Palladium (II) nitrate dihydrate ($Pd(NO_3)_2 \cdot 2H_2O$), Platinum (II) acetylacetonate ($C_{10}H_{14}O_4Pt$), Sigma-Aldrich) dissolved in 2 mL acetone (99.5%, Sigma-Aldrich) was added into 1 g of milled Fe₂O₃/ZrO₂ powders in an agata mortar followed by grinding. Finally, the impregnated powders were calcined at $600^{\circ}C$ for 2h. The total noble metal oxides loading in the as-prepared materials is around 4 wt.% of Fe₂O₃/ZrO₂ mass.

Solid oxide cell materials. SOIAB is made from an anode-supported solid oxide cell. The anode support is a composite of NiO and scandia doped ZrO_2 (ScSZ). It was prepared by dry pressing followed by dip coating. Briefly, nickel oxide (NiO), scandia stabilized zirconia (ScSZ) and carbon powders with a weight ratio of 6:4:3 were ball-milled for 4 hours in ethanol with ZrO_2 balls. Then the slurry was dried overnight in a dry oven at 80 °C. The dried powders were then fully mixed with 5 wt.% PVB in acetone with an agate mortar, followed by pressing into pellets of ϕ 1.0" and pre-sintering at 900 °C for 2h. The functional layer was deposited by dipping the pellet into a slurry containing NiO:ScSZ=6:4 (wt.%) mixture with a 10 wt.% carbon for 15 s. Then, the pellet was pulled out of the suspension and dried in an oven for 10 min. The pellet was subsequently sintered at 800 °C for 2h, after which a thin layer of ScSZ electrolyte was deposited on top of the functional layer by the same dip-coating method. The tri-layers pellets were finally co-sintered at 1350 °C for 5h. The final product was ground down to ~400 μ m thickness. The thicknesses of the ScSZ electrolyte and functional layer are ~10 μ m with ϕ 0.8".

Then the oxygen electrode (OE) was screen printed on top of the ScSZ electrolyte surface. The OE is a composite of $La_{0.8}Sr_{0.2}MnO_3$ (LSM) and $(Bi_{0.75}Y_{0.25})_{0.93}Ce_{0.07}O_{1.5}$ (BYC). It was prepared by combustion method using nitrates as the metal precursors as previously reported. ¹³ Briefly, for LSM preparation, stoichiometric amounts of $La(NO_3)_3 \cdot 6H_2O$ (Sigma-Aldrich), $Sr(NO_3)_2$ (Sigma-

Aldrich) and Mn(NO₃)₂·4H₂O (Sigma-Aldrich) were dissolved into 500 mL 0.2 M citric acid (CA, Sigma-Aldrich) solution. Then 10 mL nitric acid (70%, Sigma-Aldrich) solution was added into the mixture solution under stirring. Finally, the transparent solution was heated in an oven at 240 °C until auto-combustion. The obtained powders were then broken up and calcinated at 900 °C for 5h. The BYC powders were prepared by a similar process with Bi(NO₃)₃·5H₂O (Sigma-Aldrich), Y(NO₃)₃·6H₂O (Sigma-Aldrich), and Ce(NO₃)³·6H₂O (Sigma-Aldrich) as the metal precursors, and the calcination temperature is 700 °C. The ink consists of a mixture of LSM, BYC and a V-006 binder (Columbia International) in a weight ratio of LSM:BYC:V-006 = 40:60:150 (wt.%). After printing and drying, the cell is calcined at 800 °C for 2h to finish the cell. The effective surface area of the cathode electrode is 1.4 cm², and the silver mesh and gold paste were used as current collectors for both anode and cathode.

SOIAB assembly and testing. For a typical battery assembly, ~0.1 g energy storage materials containing 56 mg Fe were first spread over a quartz wool and then loaded into the chamber of battery holder. Then, the solid oxide cell was placed into the grove of the holder with the anode substrate facing down. A layer of glass slurry consisted of a glass powder (Schott GM31107) and binder was then applied along the perimeter between the cell and holder. The current collection wires on the anode-side were carefully routed through an insulating glass ring and the glass layer to avoid short circuiting.

The electrochemical performance of the battery was tested using a Solartron Multichannel system (model 1470e) in conjunction with a Solartron 1255 frequency response analyzer. The battery was first heated in the air from room temperature to 680 °C and held for 30 min to melt the glass and achieve gas tightness. Then, the temperature was decreased to 550 °C for testing. A 5% H_2/N_2 at 50 cm³/min was first introduced into the battery chamber for 1 hour to purge the residual air, then

switched to wet H₂ (3% H₂O) to reduce the anode and Fe-based active materials and transition metal oxide into their metallic states. After 2 hours reduction, the initial V-*j* curves and EIS of the RSOC were first measured under OCV in flowing 3% H₂O-H₂. Then the H₂ outlet and inlet valves were closed in sequence and the OCV was monitored until it reached the theoretical potential of 1.067 V (for Fe-Fe₃O₄ redox couple at 550 °C). Now the battery is ready for discharge/charge cycling. The MultiStat software is used for collecting data and performing data analysis. The cutoff voltages for discharge and charge are set at 0.8 and 2.0 V, respectively.

Materials characterization. The phase compositions of the prepared catalyst supported Fe₂O₃/ZrO₂ composites were examined by X-ray diffraction operated at a scan rate of 2° min⁻¹ from 10 to 80° using Rigaku D/MAX-2100. The morphologies of the as prepared and post tested materials were examined by a field emission scanning electron microscope (FESEM) (HITACHI, Regulus 8230) with Energy Dispersive X-Ray Spectroscopy (EDS) for elemental mapping analysis. A high-resolution transmission electron microscope (HRTEM, HITACHI H-9500). Temperature-programmed reduction (TPR) experiments were performed with a Micromeritics Chemisorption Analyzer (model 2720) in 10% H₂/Ar to study the reduction kinetics of ESU materials. A ~20 mg as-prepared material sample was placed in a quartz tube and data were collected at different ramping rates of 10 °C /min as the temperature was increased from 100 to 900 °C.

Acknowledgement

This work is supported by the National Science Foundation (NSF) under award #1801284 and the National Natural Science Foundation of China (No. 12164020). We also thank Hefei Advanced Computing Center for computational support.

References

- 1. Sepulveda, N. A.; Jenkins, J. D.; Edington, A.; Mallapragada, D. S.; Lester, R. K., The design space for long-duration energy storage in decarbonized power systems. *Nature Energy* **2021**, *6* (5), 506-516.
- 2. Hunter, C. A.; Penev, M. M.; Reznicek, E. P.; Eichman, J.; Rustagi, N.; Baldwin, S. F., Techno-economic analysis of long-duration energy storage and flexible power generation technologies to support high-variable renewable energy grids. *Joule* **2021**, *5* (8), 2077-2101.
- 3. Guerra, O. J.; Zhang, J.; Eichman, J.; Denholm, P.; Kurtz, J.; Hodge, B.-M., The value of seasonal energy storage technologies for the integration of wind and solar power. *Energy & Environmental Science* **2020**, *13* (7), 1909-1922.
- 4. Dowling, J. A.; Rinaldi, K. Z.; Ruggles, T. H.; Davis, S. J.; Yuan, M.; Tong, F.; Lewis, N. S.; Caldeira, K., Role of Long-Duration Energy Storage in Variable Renewable Electricity Systems. *Joule* **2020**, *4* (9), 1907-1928.
- 5. Albertus, P.; Manser, J. S.; Litzelman, S., Long-Duration Electricity Storage Applications, Economics, and Technologies. *Joule* **2020**, *4* (1), 21-32.
- 6. Zhu, Z.; Jiang, T.; Ali, M.; Meng, Y.; Jin, Y.; Cui, Y.; Chen, W., Rechargeable Batteries for Grid Scale Energy Storage. *Chemical Reviews* **2022**, *122* (22), 16610-16751.
- 7. Ciez, R. E.; Steingart, D., Asymptotic Cost Analysis of Intercalation Lithium-Ion Systems for Multi-hour Duration Energy Storage. *Joule* **2020**, *4* (3), 597-614.
- 8. Yuan, Z.; Liang, L.; Dai, Q.; Li, T.; Song, Q.; Zhang, H.; Hou, G.; Li, X., Low-cost hydrocarbon membrane enables commercial-scale flow batteries for long-duration energy storage. *Joule* **2022**, *6* (4), 884-905.

- 9. McKerracher, R. D.; Ponce de Leon, C.; Wills, R. G. A.; Shah, A. A.; Walsh, F. C., A Review of the Iron–Air Secondary Battery for Energy Storage. *ChemPlusChem* **2015**, *80* (2), 323-335.
- 10. Berger, C. M.; Tokariev, O.; Orzessek, P.; Hospach, A.; Fang, Q.; Bram, M.; Quadakkers, W. J.; Menzler, N. H.; Buchkremer, H. P., Development of storage materials for high-temperature rechargeable oxide batteries. *Journal of Energy Storage* **2015**, *1*, 54-64.
- 11. Leonide, A.; Drenckhahn, W.; Greiner, H.; Landes, H., Long Term Operation of Rechargeable High Temperature Solid Oxide Batteries. *Journal of The Electrochemical Society* **2014**, *161* (9), A1297.
- 12. Drenckhahn, W. W.; Greiner, H.; Kühne, M.; Landes, H.; Leonide, A.; Litzinger, K.; Lu, C.; Schuh, C.; Shull, J.; Soller, T., A Novel High Temperature Metal Air Battery. *ECS Transactions* **2013**, *50* (45), 125.
- 13. Tang, Q.; Zhang, Y.; Xu, N.; Lei, X.; Huang, K., Demonstration of 10+ hour energy storage with φ1" laboratory size solid oxide iron–air batteries. *Energy & Environmental Science* **2022**, *15* (11), 4659-4671.
- 14. Tang, Q.; Morey, C.; Zhang, Y.; Xu, N.; Sun, S.; Huang, K., Proton-Mediated and Ir-Catalyzed Iron/Iron-Oxide Redox Kinetics for Enhanced Rechargeability and Durability of Solid Oxide Iron-Air Battery. *Advanced Science* **2022**, *9* (30), 2203768.
- 15. Zhang, C.; Huang, K., An Intermediate-Temperature Solid Oxide Iron–Air Redox Battery Operated on O2—Chemistry and Loaded with Pd-Catalyzed Iron-Based Energy Storage Material. *ACS Energy Letters* **2016**, *I* (6), 1206-1211.

- 16. Zhang, C.; Huang, K., A Comprehensive Review on the Development of Solid-State Metal–Air Batteries Operated on Oxide-Ion Chemistry. *Advanced Energy Materials* **2021**, *11* (2), 2000630.
- 17. Jin, X.; Zhao, X.; Zhang, C.; White, R. E.; Huang, K., Computational Analysis of Performance Limiting Factors for the New Solid Oxide Iron-air Redox Battery Operated at 550°C. *Electrochimica Acta* **2015**, *178*, 190-198.
- 18. Tang, Q.; Ma, Y.; Huang, K., Fe3O4/ZrO2 Composite as a Robust Chemical Looping Oxygen Carrier: A Kinetics Study on the Reduction Process. *ACS Applied Energy Materials* **2021**, *4* (7), 7091-7100.
- 19. Gary J. M., Richard S. C., David J. V., Michele C. W., Bulk and key surface structures of hematite, magnetite, and goethite: A density functional theory study." *American Mineralogist* **2009**, 94(10): 1341-1350.
- 20. Tang, Q.; Huang, K., Determining the kinetic rate constants of Fe3O4-to-Fe and FeO-to-Fe reduction by H2. *Chemical Engineering Journal* **2022**, *434*, 134771.
- 21. Blöchl, P. E., Projector augmented-wave method. *Physical Review B* **1994**, *50* (24), 17953-17979.
- 22. Kresse, G.; Joubert, D., From ultrasoft pseudopotentials to the projector augmented-wave method. *Physical Review B* **1999**, *59* (3), 1758-1775.
- 23. Perdew, J. P.; Burke, K.; Ernzerhof, M., Generalized Gradient Approximation Made Simple. *Physical Review Letters* **1996**, 77 (18), 3865-3868.
- 24. Monkhorst, H. J.; Pack, J. D., Special points for Brillouin-zone integrations. *Physical Review B* **1976**, *13* (12), 5188-5192.

- 25. Grimme, S.; Antony, J.; Ehrlich, S.; Krieg, H., A consistent and accurate ab initio parametrization of density functional dispersion correction (DFT-D) for the 94 elements H-Pu. *The Journal of Chemical Physics* **2010**, *132* (15).
- 26. Anisimov, V. I.; Zaanen, J.; Andersen, O. K., Band theory and Mott insulators: Hubbard U instead of Stoner I. *Physical Review B* **1991**, *44* (3), 943-954.
- 27. Yu, X.; Li, Y.; Li, Y.-W.; Wang, J.; Jiao, H., DFT+U Study of Molecular and Dissociative Water Adsorptions on the Fe3O4(110) Surface. *The Journal of Physical Chemistry C* **2013**, *117* (15), 7648-7655.
- 28. Fan, T., Demiroglu, I, Hussein, Heider A., Liu, T. and Johnston, Roy L., DFT study of the structure, chemical ordering and molecular adsorption of Pd–Ir nanoalloys. *Phys. Chem. Chem. Phys.*, **2017**, 19, 27090.
- 29. Sun, J., Pan, Y., Xu, M., Sun, L., Zhang, S, Deng, W., and Zhai, D., Heteroatom doping regulates the catalytic performance of singleatom catalyst supported on graphene for ORR. *Nano Research*, **2024**, 17, 1086–1093.
- 30. Zhu, B, Lu, J., Sakaki, S., Catalysis of core-shell nanoparticle M@Pt (M@Co and Ni) for oxygen reduction reaction and its electronic structure in comparison to Pt nanoparticle. *Journal of Catalysis*, **2021**, 397, 13–26
- 31. Wu, X., Gao, J., Hong, Z., Lei, Z., Yun, J., Zhange, J., Xia, G., Theoretical design of bifunctional single-atom catalyst over g-C2N2 for oxygen evolution and reduction reactions. *Catalysis Today*, **2024**, 433, 114657.

32. Wang, V.; XU, N.; Liu, J.-C.; Tang, G.; Geng, W.-T., VASPKIT: A User-Friendly Interface Facilitating High-Throughput Computing and Analysis Using VASP Code, *Computer. Physics Commun.* **2021**, 267, 108033, DOI: 10.1016/j.cpc.2021.108033.

Data availability statement

The data supporting this article has been included as part of the Supplementary Information.